IEICE TRANS. COMMUN., VOL.E108–B, NO.1 JANUARY 2025

PAPER

# SAR Image Generation of 3D Target with Consideration of Complex RCS*

**Xian YU**† *and* **Yubing HAN**†a), *Nonmembers*

**SUMMARY** Synthetic aperture radar (SAR) image generation is crucial to SAR image interpretation when sufficient image samples are unavailable. Against this background, a method for SAR image generation of three-dimensional (3D) target is proposed in this paper. Specifically, this method contains three steps. Firstly, according to the system parameters, the echo signal in the two-dimensional (2D) time domain is generated, based on which 2D Fast Fourier Transform (2DFFT) is performed. Secondly, the hybrid moments (MoM)-large element physical optics (LEPO) method is used to calculate the scattering characteristics with the certain frequency points and incident angles according to the system parameters. Finally, range Doppler algorithm (RDA) is adopted to process the signal in the 2D-frequency domain with radar cross section (RCS) exported from electromagnetic calculations. These procedures combine RCS computations by FKEO solver and RDA to simulate raw echo signal and then generate SAR image samples for different squint angles and targets with reduced computational load, laying foundations for transmit waveform design, SAR image interpretation and other SAR related work.

***key words:*** *SAR image generation, RCS, 2DFFT, electromagnetic calculations, hybrid MoM-LEPO method*

## 1. Introduction

Synthetic aperture radar (SAR) refers to a certain radar system which can provide high-resolution two dimensional (2D) images in all-weather and all-time conditions [1]–[5]. Accordingly, SAR systems have been widely applied in several scenarios, e.g., resource exploration, SAR-communication integration, and military surveillance [3], [6]. Among these SAR related research, SAR image generation based on raw echo simulation is of ever-increasing importance. This is due to that on the one hand, SAR raw echo simulation taking target radar cross section (RCS) features into consideration is economic in verifying the effectiveness of waveform design and imaging algorithm; on the other hand, SAR image generation is crucial to establish a target SAR image database, which is a basic premise of SAR image interpretation including target detection and identification.

In recent literatures, several SAR image generation methods have been proposed. For instance, in [7], classic time-domain (TD) method was employed to simulate SAR raw signals, which is proved to be valid and precise but time-consuming. Additionally, with the rapid development of neural networks, the adversarial auto-encoder network aiming at few shot learning was introduced into SAR image generation in [8], [9], while this kind of network can only generate images according to the existing SAR samples but fail to generate novel SAR images. Xia, et al. studied raw echo simulation of manoeuvring targets for missile-borne SAR based on one-dimensional Fast Fourier transform (1DFFT) algorithm using the physical optics (PO)/geometrical optics (GO) and incremental length diffraction coefficients (ILDC) based RCS calculation method [10]. Similarly, [11] combines 1DFFT with time-domain shooting and bouncing ray (TDSBR) algorithm to simulate SAR raw echo signal. Overall, this 1DFFT method is computationally efficient compared with TD method, but more time-consuming than 2D frequency domain method proposed in [12]. Specifically, [12] focuses on the side-looking imaging in 2D frequency domain without consideration of target RCS as well as small and high squint angles. Furthermore, among state-of-the-art electromagnetic techniques, applying Stochastic Galerkin Method (SGM) to integral equations combined with the method of moments (MoM) has high accuracy, but requires solving a large deterministic problem [13]. Considering the high complexity and time-consuming computation of electrically large targets, large element physical optics (LEPO) method is exploited to calculate complex RCS owing to the characteristics of low complexity, faster calculation and applicability [14]–[16]. [17] elaborated in detail on the hybrid theory of MoM and PO, and successfully applied it in complex electromagnetic scattering calculations. Furthermore, considering the high complexity of electromagnetic calculations [18], FEKO as the first commercial tool for electromagnetic field analysis of 3D structures [19] is introduced to calculate RCS features. Nevertheless, the combination of RCS calculations and SAR imaging in 2D frequency domain is still missing.

To overcome the above issues, a framework of SAR image generation of 3D target with consideration of complex RCS is proposed in this paper, laying foundations for waveform design and SAR image interpretation. The contributions are listed as follows:

- The proposed method is divided into three steps, which are: (1) Simulation for raw echo in the 2D frequency domain; (2) MoM-LEPO-based RCS calculation; (3) SAR image acquisition with the matched filters on the target echo composed by step (1) and (2).
- To obtain reasonable SAR images of 3D targets, RCS is calculated via hybrid MoM-LEPO method with the parameters set according to the synthetic angle in SAR

Manuscript received February 5, 2024.
Manuscript publicized June 28, 2024.

†School of Electronic and Optical Engineering, Nanjing University of Science and Technology, Nanjing 210094, China.

*This work is supported by the National Natural Science Foundation of China under Grant 62371236.

a) E-mail: hanyb@njust.edu.cn

DOI: 10.23919/transcom.2024EBP3027

imaging system.
- Target echo with complex RCS is simulated in the 2D frequency domain, which reduces the computational load.

The remainder of the paper is organized as follows. In Sect. 2, the system model is presented, and procedures of RCS calculations and echo signal processing are also introduced. The overall flowchart is given. In Sect. 3, simulations are given to verify the effectiveness of the proposed SAR image generation. Section 4 draws the conclusion.

## 2. Analysis of the Proposed SAR Image Generation

### 2.1 Raw Echo Signal Simulation

The geometry of the airborne strip-map SAR system considered to work in the squint-looking mode is presented in Fig. 1.

As shown in Fig. 1, we assume that the radar flies at the constant height of $H$ with the speed of $v$ along the positive $Y$-direction at the depression angle $\theta$ and squint angle $\varphi$. The depression angle $\theta$ is measured from the $Z$-axis, and the squint angle $\varphi$ is measured from the $XOZ$ plane. We also assume that the target $P$, located at $(x_p, y_p, 0)$, is the radiation centre with the initial range $R_0$ and the instantaneous range between radar and the target is denoted as $R(t_a)$. The transmitted chirp signal is written as

$$s(t_r, t_a) = rect(t_r/T)\cdot w_a(t_a)\cdot \exp\left(j\pi\mu {t_r}^2\right)\cdot \exp(j2\pi f_c t_r), \tag{1}$$

where $t_r$ is the fast time, $T$ is the pulse repetition time and $rect(t_r/T)$ denotes the rectangle function, written as

$$rect(t_r/T) = \begin{cases} 1 & |t_r/T| \le 0.5, \\ 0 & \text{else}, \end{cases} \tag{2}$$

where $|\cdot|$ means the modulus operation. Also, $t_a$ is the slow time, $w_a(t_a)$ is the azimuth time envelope, $\mu$ is the chirp rate, $f_c$ is the carrier frequency.

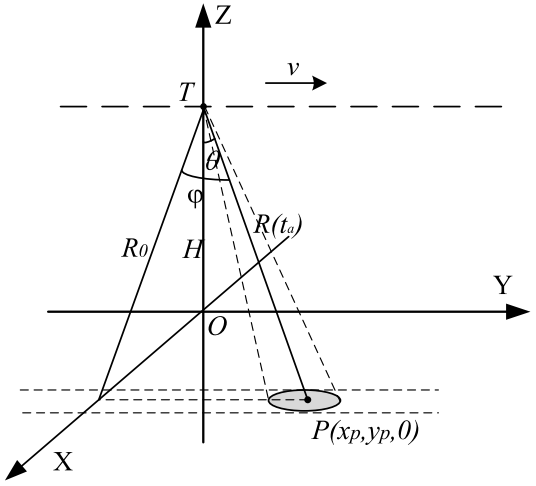


**Fig. 1** Geometric configuration of squint-looking airborne-SAR.

After demodulation to baseband, the echo reflected from the scatters can be denoted as

$$s_R(t_r, t_a, \theta, \varphi) = \sigma(t_r, \theta, \varphi) \otimes s\left(t_r - \frac{2R(t_a)}{c}, t_a\right), \tag{3}$$

where $\sigma(t_r, \theta, \varphi)$ represents the reflectivity function of $t_r$, the depression angle $\theta$ and squint angle $\varphi$, $\otimes$ denotes convolution operation, $c$ is the speed of light, and $s\left(t_r - \frac{2R(t_a)}{c}, t_a\right)$ is expressed as

$$\begin{aligned} s\left(t_r - \frac{2R(t_a)}{c}, t_a\right) =& rect\left(\frac{t_r - 2R(t_a)/c}{T}\right)\cdot w_a(t_a)\cdot \\ & \exp\left(j\pi\mu\left(t_r - \frac{2R(t_a)}{c}\right)^2\right)\cdot \exp\left(-j4\pi f_c \frac{R(t_a)}{c}\right) \end{aligned} \tag{4}$$

and $R(t_a)$ can be given as $R(t_a) = \sqrt{{R_0}^2 + v^2 {t_a}^2}$. Due to the heavy computational load of convolution in the time domain, 2DFFT is performed on (3) to convert time-domain convolution into frequency-domain multiplication so as to obtain the echo signal in the 2D frequency domain. The process of solving the 2D frequency domain expression of $s\left(t_r - \frac{2R(t_a)}{c}, t_a\right)$ is as follows.

Applying the azimuth Fourier transform into (3) and using the principle of stationary phase (POSP) yields

$$\begin{aligned} S_1(f_r, t_a, \theta, \varphi) =& \sigma(f_r, \theta, \varphi)\cdot W_r(f_r)\cdot w_a(t_a)\cdot \\ & \exp\left(-j\frac{4\pi(f_c+f_r)R(t_a)}{c}\right)\cdot \exp\left(-j\frac{\pi {f_r}^2}{\mu}\right), \end{aligned} \tag{5}$$

where $W_r(f_r)$ represents the range frequency envelope. Furthermore, it can be seen in (5) that the complex RCS $\sigma(f_r, \theta, \varphi)$ correspond to the frequency response of the scatters over frequency series $f_c + f_r$. And then, transforming (5) into the 2-D frequency domain, it can be denoted as

$$\begin{aligned} S_2(f_r, f_a, \theta, \varphi) =& A(f_r, \theta, \varphi)\cdot W_r(f_r)\cdot W_a(f_a)\cdot \\ & \exp(j\Theta(f_r, f_a))\cdot \exp\left(-j\frac{\pi {f_r}^2}{\mu}\right), \end{aligned} \tag{6}$$

where $A(f_r, \theta, \varphi)$ denotes the frequency response of the scatters in both range and azimuth directions, $W_a(f_a)$ is the azimuth frequency envelope, and $\Theta(f_r, f_a)$ is written as

$$\Theta(f_r, f_a) = -\frac{4\pi f_c R_0}{c}\sqrt{D(f_a, v)^2 + \frac{2f_r}{f_c} + \frac{{f_r}^2}{{f_c}^2}}, \tag{7}$$

where

$$D(f_a, v) = \sqrt{1 - \frac{c^2 {f_a}^2}{4v^2 {f_c}^2}}. \tag{8}$$

For further analysis, (7) can be expanded to Taylor's series at $f_r = 0$

$$\Theta(f_r, f_a) = -\frac{4\pi f_c R_0}{c} \left( D(f_a, v) + \frac{f_r}{f_c D(f_a, v)} - \frac{{f_r}^2}{2{f_c}^2 D(f_a, v)^3} \frac{c^2 {f_a}^2}{4v^2 {f_c}^2} \right). \quad (9)$$

It follows then that the items in (6) apart from $A(f_r, \theta, \varphi)$ can be simulated according to the system parameters. Therefore, RCS calculations are crucial in echo simulation of target in the 2D frequency domain. Based on complex RCS, it is noted that LFM can be replaced by other waveforms by changing the weights of different frequency points through FFT on the waveform. In this paper, we take LFM as an example and design the corresponding matched filters.

### 2.2 MoM-LEPO-Based RCS Calculations

Turntable imaging is a powerful tool for the calculations of scattering properties of targets [20], [21]. The scattering characteristics are simulated over the depression angle $\theta$ and rotation angle $\alpha$ centring on the squint angle $\varphi$. The top view is given in Fig. 2. Specifically, the down-range is defined as the axis parallel to the direction of incidence, with a frequency series $f_0 + f_r$ and the cross-range is perpendicular to the down-range.

The frequency response $A(f_r, \theta, \varphi)$ after discretized to an $M \times N$ matrix is composed of

$$A(f_r, \theta, \varphi) = \begin{pmatrix} A(f_1, \theta, \beta_1) & A(f_2, \theta, \beta_1) & \dots & A(f_N, \theta, \beta_1) \\ A(f_1, \theta, \beta_2) & A(f_2, \theta, \beta_2) & \dots & A(f_N, \theta, \beta_2) \\ \vdots & \vdots & \vdots & \vdots \\ A(f_1, \theta, \beta_M) & A(f_2, \theta, \beta_M) & \dots & A(f_N, \theta, \beta_M), \end{pmatrix} \quad (10)$$

where $\beta_j, j = 1, 2, \dots, M$ is the sampling point of the rotation angle $\alpha$ centered on the squint angle $\varphi$, and $f_i, i = 1, 2, \dots, N$ is the sampling point of the frequency series $f_c + f_r$. Electromagnetic scattering calculations can be seen as the projection of the 3D model on the plane formed by the incident angle. And the reflectivity function $\sigma(t_r, \theta, \varphi)$ can be generated with 2D inverse fast Fourier transform (2DIFFT) on $A(f_r, \theta, \varphi)$ when the rotation angle is relatively small. Specifically, to make the RCS features reasonable in SAR imaging, The rotation angle $\alpha$ should be equal to the synthetic angle in SAR imaging, based on which $\alpha$ is represented by

$$\alpha = 0.886 \frac{\lambda}{L_a}, \quad (11)$$

and the interval of the incident angle is

$$\Delta\beta = \frac{\alpha}{N - 1}. \quad (12)$$

Considering the squint angle $\varphi$, and the incident angles $\beta_j$ are denoted by

$$\beta_j = (j - 1) \cdot \Delta\beta + \varphi - \frac{\alpha}{2}. \quad (13)$$

MoM is a suitable approach for addressing electromagnetic scattering problems with arbitrary geometrical shapes in the lower frequency range. However, as the frequency increases, the computational time and memory requirements often surpass the capabilities of available computers. In addition, for a scatterer with large and smooth surfaces, LEPO method can be modelled using large triangular edge elements. This is achieved by incorporating asymptotic solutions to predict the rapid phase dependence of the unknown current distribution. This yields a slowly varying residual function that can be represented by a coarse density of unknowns. This is akin to an arbitrary field incident on a planar surface, where the phase of the induced current on the surface can be approximated from the phase of the incident field [14], [15]. In hybrid scatters, the rough surface and target RCS often exhibit inconsistencies. The surface is typically electrically large and relatively smooth, while the target is usually smaller in size and contains intricate structures. It is challenging to model such disparate electrical structures accurately using one single method. Therefore, by employing MoM-LEPO hybrid method, the regions can be divided and discretized into different scales to reduce the number of elements for the electrically large surfaces. The coupling effects between different regions are then computed, enabling a relatively accurate calculation of the scattering field while significantly reducing the computational time and memory consumption. To demonstrate the above analysis, we have calculated the RCS of a one-meter diameter metal sphere via these methods, respectively. The simulation results are listed as in Table 1.

The RCS of a one-meter diameter metal sphere has a true value of $\pi/4$. Simulation results in Table 1 indicate that the MoM method achieves the highest accuracy but requires significant memory and time resources. On the other hand, the PO method has lower memory requirements and faster computation time but produces considerable errors. By employing a MoM-LEPO hybrid approach, the computational

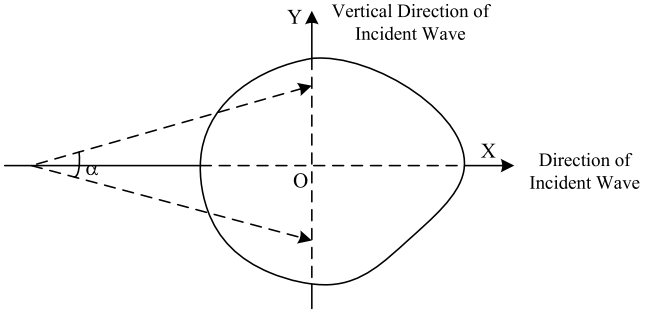


**Fig. 2** Sketch map of incident wave direction in electromagnetic calculations.

**Table 1** Comparison of different electromagnetic computation methods.

| Methods | MoM | PO | MoM-LEPO |
|---|---|---|---|
| RCS /$m^2$ | 0.788 | 0.762 | 0.769 |
| Error rate | 0.3% | 3.0% | 2.1% |
| Memory /GB | 19.4 | 0.05 | 0.06 |
| Time /$s$ | 10016.6 | 3.5 | 3.8 |

accuracy can be improved while utilizing lower memory and time resources. This makes it suitable for calculation complex RCS of electrically large objects. Hence, we utilize the hybrid MoM-LEPO method for RCS calculations in this work.

### 2.3 SAR Image Generation

With the target RCS $A(f_r, \theta, \varphi)$ substituted in (7), raw echo signal in the 2-D frequency domain is simulated. RDA, characteristic of simple and efficient, is adopted to obtain the SAR image. The specific details are referred to [22]. The focused SAR imaging result is given by

$$s_{img}(t_r, t_a, \theta, \varphi) = \sigma(t_r, \theta, \varphi) \cdot sinc\left(\frac{t_r - 2R_0/c}{T}\right) \cdot sinc(B_a t_a), \tag{14}$$

where $B_a$ represents the Doppler bandwidth.

### 2.4 Overall Flowchart

Based on the above analysis, the procedures are given as in Fig. 3, which illustrates the whole process of the proposed SAR image generation method with fast RCS calculation speed assisted by MoM-LEPO and low computational load via 2DFFT. Basically, there are three steps and the details are as follows.

- Step 1: Raw echo simulation. According to the SAR system parameters, raw echo signal in the 2D frequency domain is generated after performing 2DFFT.
- Step 2: MoM-LEPO-based RCS calculation. To calculate the target RCS, electromagnetic calculation in aid of hybrid MoM-LEPO method is carried out with the frequency points in Step 1 and the derived incident angles.
- Step 3: SAR image acquisition. By substituting the target RCS in Step 2 into the raw echo in the 2D frequency domain in Step 1, the echo reflected from the target in the 2D frequency domain is obtained. With the matched filters derived in RDA, SAR image of the target is acquired.

## 3. Simulations and Results

### 3.1 Results and Discussion

Based on the above analysis and fundamentals of SAR imaging [22], experiments are carried out using the system parameters listed in Table 2 to verify the efficiency of the proposed SAR image generation method.

Figure 4 illustrates the 3D generic aeroplane model a380 with a size of 72.44 m × 75.41 m × 23.45 m to perform RCS calculations.

We choose the squint angle $\varphi = 0^{\circ}, 5^{\circ}, 25^{\circ}$ to verify that the proposed method is feasible when SAR works in the side-looking and squint-looking mode. And the relevant parameters are listed as follows. We take $\varphi = 0^{\circ}$ as an example. Under this circumstance, $\alpha = 0.886\lambda/L_a = 3.1728^{\circ}$, $\beta_1 = -1.5864^{\circ}$ and $\beta_N = 1.5864^{\circ}$. With the certain incident angle settings and hybrid MoM-LEPO method, the normalized RCS (NRCS) curve of the aeroplane for $f_c = 4$ GHz

**Table 2** System parameters.

| Parameters | Values |
|---|---|
| Depression Angle $\theta$ [°] | 30 |
| Carrier Frequency $f_c$ [GHz] | 4 |
| Chirp Rate $\mu$ [Hz/s] | $6 \times 10^{13}$ |
| Pulse Repetition Time [$\mu s$] | 2 |
| Chirp Bandwidth [MHz] | 120 |
| Initial Range $R_0$ [km] | 20 |
| Velocity $v$ [m/s] | 120 |
| Antenna length [m] | 1.2 |
| Number of Range Samples | 1024 |
| Number of Azimuth Samples | 2048 |
| Range Oversampling Rate | 1.2 |
| Azimuth Oversampling Rate | 1.25 |
| Polarization mode | HH |
| Normalized linear magnitude | [0,1] |

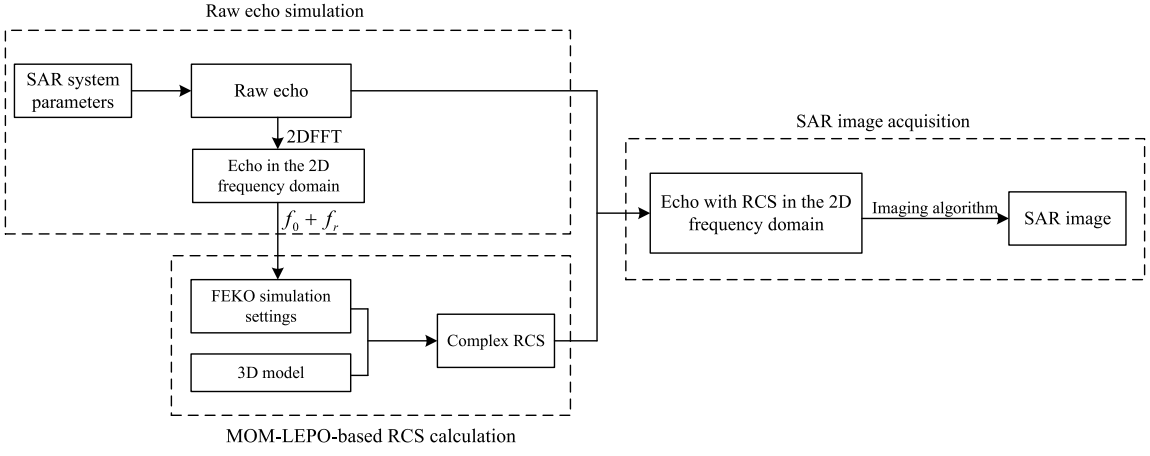


**Fig. 3** Flowchart of SAR image generation for a 3D target with consideration of RCS.

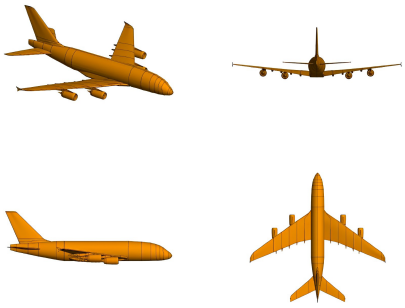

**Fig. 4** 3D aeroplane model.

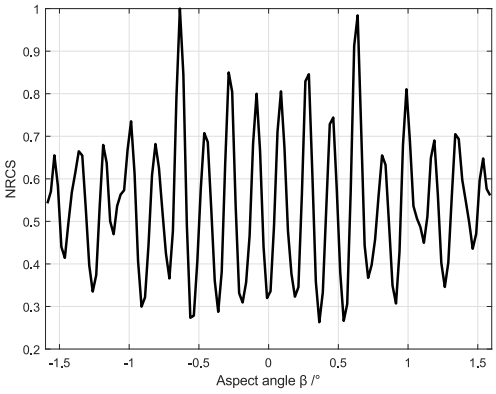


**Fig. 5** NRCS vs aspect angle $\beta$ for $\varphi = 0°$.

is shown in Fig. 5. According to Fig. 5, the RCS curve is symmetric about $\beta = 0°$, which is consistent with the symmetric structure of the aeroplane. Additionally, RCS value over certain incident angle is relatively small. For example, when $\beta = 0°$, the scattering properties are not intense in this direction compared with those in other directions.

As stated in [23], [24], HRRP can be used in approximately estimating the locations and intensities of the scattering points composed by important parts of the target, conducive to target recognition and detection. With the RCS curve in Fig. 5, we perform IFFT on the RCS data when $\beta = 0°$ to obtain high resolution range profile (HRRP) as shown in Fig. 6. Under the incident angle $\theta = 30°, \phi = 0°$, the peaks of HRRP for the aeroplane reveals the existence of crucial parts, such as nose, fuel tanks, landing gear, wings and tail. Furthermore, the distance between peaks and the actual distance between components are proportional. For example, the distance between nose and tail is approximately equal to the product of length of the plane and $\sin\theta$, which means that the HRRP can be viewed as the projection of the 3D target in the incident direction of plane wave.

Considering that HRRP in Fig. 6 displays the key components of the aeroplane along the range axis, the azimuth position of which can be obtained with the inclusion of the rotation angle. Thus, HRRP for the incident angles within the rotation angle $\alpha$ set according to the value of squint angle $\varphi$ will constitute for RCS of the aeroplane. In other words, by performing 2DIFFT on frequency response $A(f_r, \varphi, \theta)$ denoted as (10), RCS can be obtained, revealing the scat-

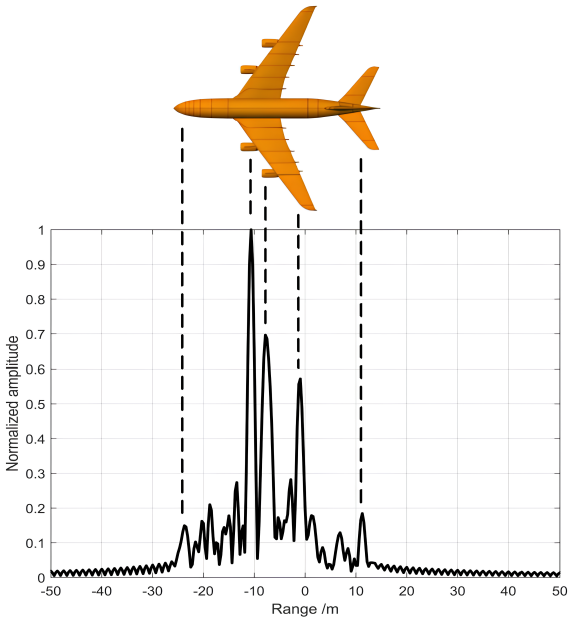


**Fig. 6** HRRP of the aeroplane.

tering characteristics of the aeroplane. As shown in Fig. 7, the important components of an aeroplane, such as nose, wings, landing gear and tail, can be vividly seen. Besides, the scattering characteristics on the central axis of the aircraft are not intense in Fig. 7(a), which is consistent with the finding for $\beta = 0°$ in Fig. 5. Furthermore, RCS show that the aeroplane tilts with different incident angles caused by increasing squint angle $\varphi$, verifying that RCS calculation similar to turntable imaging can be seen as the projection of the 3D target in the incident direction.

Based on the LFM transmitted signal and target RCS, raw echo signal in the 2-D frequency domain is simulated. By multiplying the matched filters, SAR images for different squint angles are shown in Fig. 8. We observe that the strong scattering points in SAR images are consistent with original RCS, also revealing the crucial parts of the aeroplane model. This means that through the proposed SAR image generation method, SAR image samples for different models and angles can be generated. Furthermore, the aeroplane in the SAR image tilts for a certain squint angle compared with the corresponding RCS.

Considering that the target SAR imaging can be seen as the amplitude and phase modulation of the reference point, we resort to the amplitude spectrum slice by upsampling $32 \times 32$ points centered around the reference point by 8 times for different squint angles to explain the tilt of SAR images in Fig. 9. To make a better comparison of RCS and SAR images, the azimuth sidelobes are parallel to the azimuth axis. Since that the Doppler centroid frequency is $2(f_c + f_r)\, v \sin\varphi / c$, the sampling point of azimuth frequency is related to the range frequency $f_r$. This leads to the tile of the range spectrum, i.e., as the squint angle $\varphi$ increases, the range sidelobes tilt more away from the horizontal axis.

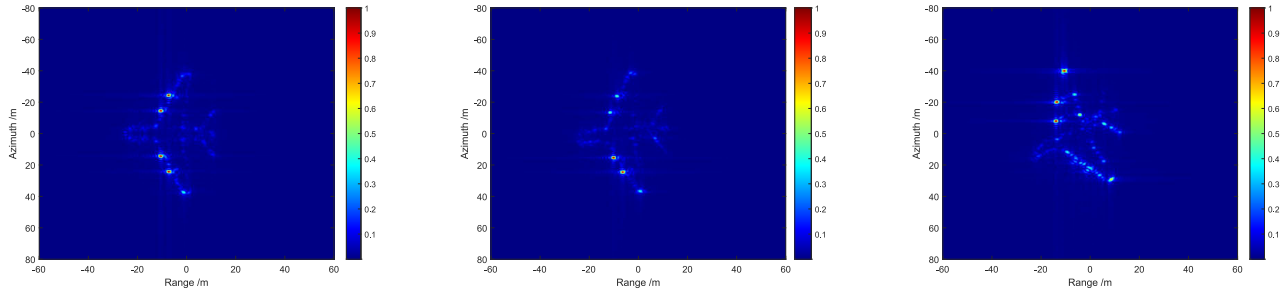


(a) $\varphi = 0°$ (b) $\varphi = 5°$ (c) $\varphi = 25°$

**Fig. 7** RCS of the aeroplane for different squint angles.

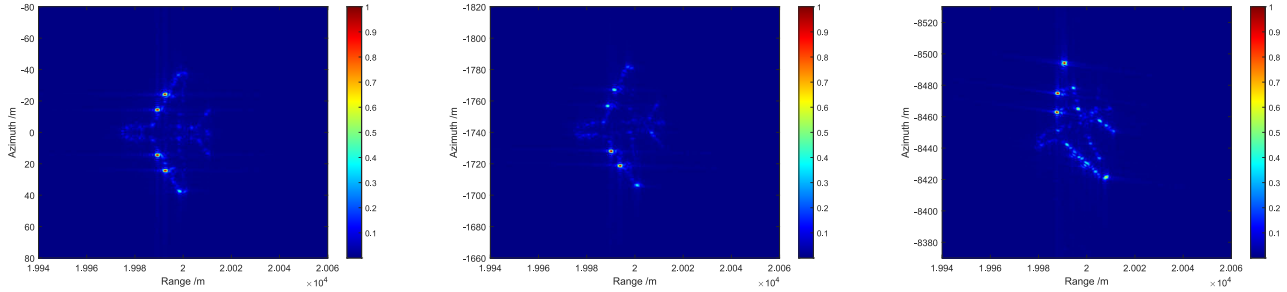


(a) $\varphi = 0°$ (b) $\varphi = 5°$ (c) $\varphi = 25°$

**Fig. 8** SAR image with LFM transmitted signal for different squint angles.

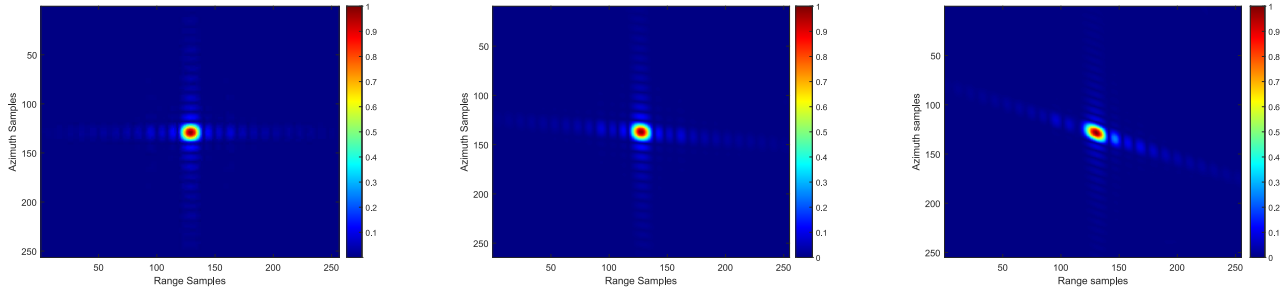


(a) $\varphi = 0°$ (b) $\varphi = 5°$ (c) $\varphi = 25°$

**Fig. 9** Amplitude spectrum slice centered around the reference point for different squint angles.

### 3.2 Computational Efficiency Analysis

According to [7], the computational efficiency of TD method is denoted as

$$C_{TD} = M^2N^2. \tag{15}$$

Comparatively, raw echo simulation based on 1DFFT proposed by [10] and [11] reduces the computational complexity, which can be written as

$$C_{1DFFT} = MNC_R + 1/2MNlog_2(N) + MN \tag{16}$$

where $C_R$ represents the complexity for computing single frequency RCS of the whole target, and $1/2MNlog_2(N)$ denotes IFFT operation. Comparatively, the proposed 2DFFT method omits this step and perform range and azimuth compensation in the frequency domain. Thus, the computational load is reduced to

$$C_{total} = MNC_R + MN. \tag{17}$$

Comparatively, it is evident that the proposed method has a lower computational complexity, which would improve the efficiency of SAR image generation and lays a foundation for waveform design and SAR image interpretation.

## 4. Conclusion

This work presents a framework of SAR image generation for a 3D target in aid of hybrid MoM-LEPO electromagnetic calculations, which lays the foundation for radar waveform design and SAR image interpretation. Specifically, multiplying raw echo signal after 2DFFT and MoM-LEPO-based RCS yields target echo in the 2D frequency domain, based on which SAR image is generated via RDA. This

method reduces computational load and speed up calculation by performing 2DFFT in raw echo signal and using FEKO solver. Furthermore, simulation results show that the proposed method is applicable in different squint angles.

## Acknowledgments

This work is supported by the National Natural Science Foundation of China under Grant 62371236.

### References

[1] H. Huang, F. Gao, J. Wang, A. Hussain, and H. Zhou, "An incremental SAR target recognition framework via memory-augmented weight alignment and enhancement discrimination," IEEE Geosci. Remote Sens. Lett., vol.20, 4005205, 2023.
[2] Y. Yuan, S. Chen, S. Zhang, and H. Zhao, "A chirp scaling algorithm for forward-looking linear-array SAR with constant acceleration," IEEE Geosci. Remote Sens. Lett., vol.15, no.1, pp.88–91, Jan. 2018.
[3] C. Wang, S. Luo, J. Pei, X. Liu, Y. Huang, Y. Zhang, and J. Yang, "An entropy-awareness meta-learning method for SAR open-set ATR," IEEE Geosci. Remote Sens. Lett., vol.20, 4005105, 2023.
[4] R.V. Fonseca, R.G. Negri, A. Pinheiro, and A. Atto, "Wavelet spatio-temporal change detection on multitemporal SAR images," IEEE J. Sel. Topics Appl. Earth Observ., vol.16, pp.4013–4023, 2023.
[5] J. Chen, M. Xing, X.G. Xia, J. Zhang, B. Liang, and D.G. Yang, "SVD-based ambiguity function analysis for nonlinear trajectory SAR," IEEE Trans. Geosci. Remote Sens., vol.59, no.4, pp.3072–3087, April 2021.
[6] R. Hu, B.S.M.R. Rao, A. Murtada, M. Alaee-Kerahroodi, and B. Ottersten, "Automotive squint-forward-looking SAR: High resolution and early warning," IEEE J. Sel. Topics Signal Process., vol.15, no.4, pp.904–912, June 2021.
[7] A. Mori and F. De Vita, "A time-domain raw signal simulator for interferometric SAR," IEEE Trans. Geosci. Remote Sens., vol.42, no.9, pp.1811–1817, Sept. 2004.
[8] Q. Song, F. Xu, and Y.Q. Jin, "SAR image representation learning with adversarial autoencoder networks," IGARSS 2019 - 2019 IEEE Int. Geosci. and Remote Sens. Symp., Yokohama, Japan, pp.9498–9501, IEEE, July 2019.
[9] Q. Song, H. Chen, F. Xu, and T.J. Cui, "EM simulation-aided zero-shot learning for SAR automatic target recognition," IEEE Geosci. Remote Sens. Lett., vol.17, no.6, pp.1092–1096, June 2020.
[10] W. Xia, Y. Qi, L. Huang, and X. Jin, "Missile-borne SAR raw signal simulation for maneuvering target," Int. J. Antennas Propag., vol.2016, pp.1–12, 2016.
[11] C.l. Dong, X. Meng, and L.x. Guo, "Research on SAR imaging simulation based on time-domain shooting and bouncing ray algorithm," IEEE J. Sel. Topics Appl. Earth Observ., vol.16, pp.1519–1530, 2023.
[12] R. Li, K. Ji, H. Zou, and S.L. Zhou, "Simulation of SAR imagery of target based on electromagnetic scattering characteristic computation," Radar Sci. and Technol., vol.22, no.5, pp.395–400, 2010.
[13] T. El-Moselhy and L. Daniel, "Variation-aware stochastic extraction with large parameter dimensionality: Review and comparison of state of the art intrusive and non-intrusive techniques," 2011 12th International Symposium on Quality Electronic Design, pp.1–10, 2011.
[14] N.K. Sahoo, D.C. Panda, and S.K. Dash, "RCS studies of anti-ship missile over sea surface using LE-PO method," 2017 IEEE Appl. Electromagn. Conf. (AEMC), pp.1–2, 2017.
[15] A. Altintas and A. Celik, "Large flat plate models in the physical optics method for RCS calculations," 10th Int. Conf. on Math. Methods in Electromagn Theory, 2004., pp.586–588, 2004.
[16] H. Mohammadzadeh, A.Z. Nezhad, and Z.H. Firouzeh, "Modified physical optics approximation for RCS calculation of dielectric coated PEC with axial symmetry," 2013 21st Iranian Conf. on Elect. Eng. (ICEE), pp.1–5, 2013.
[17] U. Jakobus and F. Landstorfer, "Improved PO-MM hybrid formulation for scattering from three-dimensional perfectly conducting bodies of arbitrary shape," IEEE Trans. Antennas Propag., vol.43, no.2, pp.162–169, 1995.
[18] Q. Chang, C. Sun, and Y. Wang, "RCS measurement method based on high-resolution sparse turntable imaging," 2018 Int. Conf. on Microwave and Millimeter Wave Technology (ICMMT), Chengdu, pp.1–3, IEEE, May 2018.
[19] X. Wang, C. Wang, and Y. Liu, "RCS computation and Analysis of target using FEKO," Proc. of 2014 3rd Asia-Pacific Conf. on Antennas and Propag., Harbin, China, pp.822–825, IEEE, July 2014.
[20] X. Lu, J. Xia, Z. Yin, and W. Chen, "High resolution turntable radar imaging via two dimensional deconvolution with matrix completion," Sensors, vol.17, no.3, p.542, March 2017.
[21] S. Demirci, "Applying polarimetric target decomposition to 2D turntable ISAR imagery of a complex vehicle," Int. J. Antennas Propag., vol.2022, pp.1–15, July 2022.
[22] I.G. Cumming and F.H. Wong, Digital Processing of Synthetic Aperture Radar Data: Algorithms and Implementation, Artech House, Norwood, 2005.
[23] W. Yue and Y. Xin, "Performance analysis of radar high-resolution range profiling for stationary targets," 2017 IEEE Int. Conf. on Signal Process., Commun. and Comput. (ICSPCC), Xiamen, pp.1–5, IEEE, Oct. 2017.
[24] L. Du, H. Liu, Z. Bao, and M. Xing, "Radar HRRP target recognition based on higher order spectra," IEEE Trans. Signal Process., vol.53, no.7, pp.2359–2368, July 2005.

**Xian Yu** was born in 1997. She received the B.S. degree in electronic engineering from Nanjing University of Science and Technology, China, in 2019, where she is currently pursuing the Ph.D. degree. Her research interests include SAR imaging, maritime target detection and radar signal processing.

**Yubing Han** was born in 1971. He received the Ph.D. degree in signal and information processing from Southeast University, China, in 2006. Since 2006, he has been a Faculty Member with the School of Electronic and Optical Engineering in Nanjing University of Science and Technology, where he is currently a Professor. His current research interests include SAR imaging, sensor signal processing, radar signal processing, wireless communications, and digital image processing.